RESEARCH ARTICLE | APRIL 10 2025

Magnetic resonance velocimetry shows detailed flow patterns in open microchannels

Georges C. Saliba ✉ ⓘ ; Jan G. Korvink ⓘ ; Juergen J. Brandner ⓘ

Check for updates

View Online   Export Citation

Articles You May Be Interested In

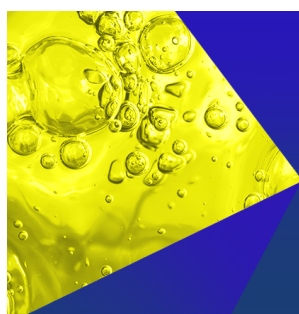The impact of thixotropic behavior on microfluidic mixing in a staggered-herringbone mixer

Physics of Fluids (April 2024)

Continuous flow microreactor for protein PEGylation

Biomicrofluidics (August 2018)

Electrical and optical properties of Ta-Si-N thin films deposited by reactive magnetron sputtering

J. Appl. Phys. (December 2012)

Magnetic resonance velocimetry shows detailed flow patterns in open microchannels

View Online   Export Citation   CrossMark

Georges C. Saliba,[1,a)] (iD) Jan G. Korvink,[1] (iD) and Juergen J. Brandner[1,2] (iD)

AFFILIATIONS

[1]Institute of Microstructure Technology (IMT), Karlsruhe Institute of Technology (KIT), Hermann-von-Helmholtz-Platz 1,
 76344 Eggenstein-Leopoldshafen, Germany
[2]Karlsruhe Institute of Technology, Karlsruhe Nano Micro Facility KNMFi, Hermann-von-Helmholtz-Platz 1,
 76344 Eggenstein-Leopoldshafen, Germany

[a)]Author to whom correspondence should be addressed: georges.saliba@kit.edu

ABSTRACT

Open microchannels facilitate gas–liquid contact. This unit operation has many uses in industrial and medical processing, generally requiring gravity-driven falling liquid films. Modulation of the microchannel geometry, either through smooth cross-sectional waviness or using herringbone structures, can achieve optimal surface-to-volume ratios, increase gas–liquid contact, and provoke chaotic mixing. Using non-intrusive magnetic resonance velocimetry, we reveal the internal three-dimensional flow profiles and confirm vortex-driven mixing patterns. The wavy channels affected the shape of the gas/liquid interface, especially at lower flow rates for which slight improvement in the surface-to-volume ratio was observed. The open-channel micromixers were most effective for higher groove depth to film thickness ratios. The deeper the grooves, the more prominent the mixing vortices were, which is also the case for closed-channel micromixers.

I. INTRODUCTION

Falling-film microreactors are widely used in chemistry with applications in CO_2 capture,[30] fluorination,[16] chlorination,[11] sulfonation,[27] and hydrogenation.[29] They produce liquid films having typical thicknesses of tens to hundreds of micrometers with a maximum width of around 1 mm. At this scale, small quantities of hazardous or expensive liquids can be handled continuously with reduced risk. In addition, open flows in microchannels have a large specific interfacial area, which implies an efficient gas absorption and penetration through the film. Reducing the size of the flow improves both absorption and diffusion times.

Scale reduction, however, comes at a cost. Because turbulence is usually absent, mass transport occurs predominantly by intermolecular diffusion. The efficiency of diffusion is dictated by three factors: the diffusion rate D, the interfacial surface area A, and the concentration gradient ∇c. Setting aside the diffusion rate, which can be improved by increasing the temperature, one way of increasing the interfacial area and the concentration gradient involves patterning the channel.

If the geometry of the cross section changes in the streamwise direction, then the shape of the free surface departs from that of a plain meniscus. In the present study, all three walls of a rectangular channel have a sinusoidal shape in the flow direction to change the cross section of the film. Since surface tension predominates at this scale, the film will be stretched and compressed if the distance between the walls fluctuates. In other words, the film is thinned out and then pushed together along the vertical axis. This leads to continuous variations in the thickness of the film which gives its surface a complex topology. As a side-effect, the fluctuations in velocity result in additional shear stress in the flow, which in turn increase dispersion, but only along the streamlines. This effect is called Taylor–Aris dispersion. Nevertheless, this type of flow will not contribute to mixing in the transverse direction, i.e., in the cross section of the film.

The literature on micromixers mainly focuses on closed microchannels. Jen *et al.*[17] investigated mixing in a T-mixer and compared it to inclined, oblique, and wave-like mixers. These three designs featured twisted geometries with the aim of inducing chaotic advection. Numerical simulation revealed that the inclined mixer yields the shortest mixing lengths, since the flow sways at a large amplitude.

Strook *et al.*[23] patterned the bottom of a microchannel with staggered-herringbone motifs using planar lithography to induce chaotic mixing in the flow. The fluid flows into these grooves which are placed across its flow path at an angle. This in turn induces a

TABLE I. Geometric parameters of the variable-cross section channels.

Name	Geometry designation	Period (μm)	Amplitude (μm)	Phase shift ($\times 2\pi$)
Long wavelength	LW-PH0	750	100	0
	LW-PH25	750	100	0.25
	LW-PH50	750	100	0.5
Short wavelength	SW-PH0	430	100	0
	SW-PH25	430	100	0.25
	SW-PH50	430	100	0.5

transverse flow component which then develops into circulating flow. In other words, two vortices appear in the transverse plane whose separating line moves back and forth. A series of studies followed that investigated the geometric parameters affecting mixing efficiency. Aubin et al.[5] showed that the groove depth and the groove width have the greatest influence on homogenization, unlike the number of grooves per cycle which had no effect. While deeper grooves resulted in better mixing, the researchers found that an intermediary value of the groove width was optimal, i.e., neither too narrow nor too wide. In their case, the groove depth to channel height ratios were $\alpha = 0.30$–0.35. Du et al.[9] performed simulations where they varied the value of α both by fixing the channel height and changing the groove depth, and vice versa. They found that if α increases, the mixing length decreases, and the decrease is more substantial when the height of the channel was decreased as opposed to when the grooves were deepened. Since the flow is laminar inside the grooves, if they are too deep, the overall mixing efficiency deteriorates. Subsequent studies corroborated these findings over the years.[3,18,28]

The staggered-herringbone mixer was also used for open-channel flows in the context of falling-film microreactors.[1,2,31] However promising, these studies relied either on flow simulations or on analyzing the liquid at the outlet of the system to evaluate the performance of the microreactor.

Aubin et al.[4] performed numerical simulations of the diagonal and staggered-herringbone micromixers proposed originally by Stroock et al.[23] in a closed-channel configuration. They observed, among other things, that the geometry of the bas-relief had little effect on the pressure drop. They also showed that the deformation rate does not correctly quantify mixing and stretching. Although diagonal and staggered-herringbone mixers show clearly different mixing behaviors, the deformation rates and their distributions were similar in both.

Numerical simulations by Schönfeld and Hardt[22] demonstrated that the transverse component of velocity in micromixers with slanted grooves is weakly dependent on the Reynolds number. However, they showed that replicating the pattern on the opposite channel wall clearly increased the transverse component of velocity.

In what follows, we present results pertaining to two different designs: open microchannels with variable depths and widths, and open-channel micromixers. Periodic changes in depth and width result in a repeating acceleration and deceleration of the flow that causes Taylor–Aris dispersion, which acts along the streamlines. In the context of gas–liquid contactors, we need to enhance mass transport across the depth of the film and not so much in the axial flow direction, so we chose to focus here on the effect of a variable cross section on the shape of the gas–liquid interface and the surface-to-volume ratio. In the second part of the results section, we look at the flow inside of open-channel micromixers with different groove depths. Since we are dealing with an open-channel flow, the height of the liquid also changes with the volumetric flow rate. This study is the first to extensively investigate falling films at the microscale using magnetic resonance velocimetry and is an extension of the work presented in Saliba et al.[20,21] Unlike the work presented in Saliba et al.,[20] the channels in the first part of the present study have a variable cross section along the axial direction. In the present study, we focus on experimental results, since most of the aforementioned studies resort to computational fluid dynamics (CFD) simulations to investigate the flow because it was not possible to measure the velocity field experimentally.[2,6–8] Magnetic resonance velocimetry enables us to fill that gap in the literature on falling films in microchannels.

II. MATERIALS AND METHODS
A. Magnetic resonance velocimetry

The most common velocity measurement techniques trace their origins back to the work of Prandtl, who, in one of his experiments, introduced aluminum particles onto the surface of water to bring out the motion of the fluid. Seeding particles and optical measurements still underlie, in different ways, techniques such as particle image velocimetry or laser Doppler velocimetry.

On the other hand, magnetic resonance velocimetry is based on the behavior of nuclear spins subjected to a strong magnetic field. To understand how this technique works, an analogy with a spinning top is instructive. Neglecting all losses, a spinning top remains upright. When tilted, it will begin to precess around the vertical axis before gradually returning to the upright position. Similarly, a spin ensemble will align with a strong magnetic field and is tilted by an appropriate radio frequency (RF) signal. When the RF signal is turned off, the nuclear spins will return to alignment, sending out a measurable signal. The emitted signals will differ, depending on the environment of the nuclear spins and on the magnetic field experienced by the sample in time and space. In this way, information such as spatial position and velocity can be encoded into the signal.

A common method to measure velocity using Nuclear Magnetic Resonance (NMR) is to encode the motion into the phase of the spin magnetization. In this case, spins act as magnetic moments, and as they travel through a magnetic field gradient, their precession rate experiences a related phase shift, which manifests itself in the phase of the magnetization. If the magnetic field gradient is linear, the phase shift gained in unit time is proportional to displacement and hence velocity in the gradient direction. This technique offers a direct velocity measurement from the moving fluid's nuclei, unlike hot-wire

velocimetry, where velocity is deduced from the cooling of a heated wire, or Particle Image Velocimetry (PIV) and Particle Tracking Velocimetry (PTV), which measure the speed of the seeding particles and not that of the fluid itself.

Magnetic resonance imaging and nuclear magnetic resonance spectroscopy are closely associated with the fields of medicine and chemistry, respectively. However, the same underlying principles can be used to perform velocity measurements on systems of interest to engineers. Magnetic resonance velocimetry has been successfully used to study turbulent flow in a variety of engineering applications.[12,13]

Encoding velocity and then obtaining a signal consist in applying a sequence of radio frequency pulses and timed magnetic field gradients. The sequence then leads to a radio frequency echo from the sample that the receiver coil picks up. The radio frequency pulses and the magnetic field gradients in the x, y, and z directions overlap in order to perform operations such as slice selection (choosing the plane of measurement), velocity encoding, and spatial encoding for the in-plane location. Nuclei with non-zero magnetic moments subjected to a strong magnetic field B_0 will start precessing at the Larmor frequency ω_0 given by

$$\omega_0 = \gamma B_0, \tag{1}$$

where γ is the gyromagnetic ratio which is a characteristic of the nucleus. If we apply a linear magnetic field gradient $G\,(\mathrm{mTm}^{-1})$ (which could be time-dependent, i.e., $G = G(t)$) along a given direction, say x, the precession frequency (how fast the tilted spinning top rotates around the vertical axis) will depend on the positions of the nuclei according to

$$\omega_0(x) = B_0 + G \cdot x. \tag{2}$$

The position x of a nucleus can in turn be expanded as

$$x(t) = x_0 + \frac{dx}{dt}t + \frac{1}{2!}\frac{d^2x}{dt^2}t^2 + \frac{1}{3!}\frac{d^3x}{dt^3}t^3 + \cdots, \tag{3}$$

$$= x_0 + vt + \frac{1}{2!}at^2 + \frac{1}{3!}jt^3 + \cdots, \tag{4}$$

where v is velocity, a is acceleration, and j is jerk. The phase that the nucleus accumulates during a time t is given by

$$\varphi(x,t) = \gamma \int_0^t (B_0 + G(\tau) \cdot x(\tau))d\tau, \tag{5}$$

$$= \gamma \int_0^t [B_0 + G(\tau) \cdot (x_0 + v\tau + \cdots)]d\tau. \tag{6}$$

If the time-dependent gradient $G(t)$ has a net area of zero and if we ignore the higher order moments $\int_0^t \tau^n G(\tau)d\tau$ for $n > 1$, then phase is proportional to velocity

$$\varphi = \gamma M_1 v, \tag{7}$$

where $M_1 = \int_0^t \tau G(\tau)d\tau$. In sum, if the sample experiences a spatial magnetic field gradient, the phase will depend on the position. A well-designed time-dependent gradient creates in turn a linear relationship between velocity and the phase of the spin. What was presented so far is only an outline of the theory underlying magnetic resonance velocimetry using phase encoding. The reader is referred to specialized texts for a more extensive presentation of the topic.[12,13]

In the present study, a standard cartesian 4D magnetic resonance velocimetry (MRV) sequence ("FLOWMAP," ParaVision 6.0.1, Bruker BioSpin MRI GmbH, Ettlingen, Germany) was used. The sequence was composed of a three-dimensional gradient-echo and a 4-point Hadamard velocity encoding scheme.[10] For each case, the measurements are repeated 40–50 times and then averaged. The field of view (FOV) was 5 mm × 5 mm with 150 points in each direction. The resolution in the $xy-$ plane was then 33 μm. The resolution in the $z-$ direction depended on the wavelength P (see Fig. 1). It was chosen in a way to have around 20 slices per period of the sine pattern. Worth mentioning that the partial volume effect (cf. Saliba *et al.*[20]) is a source of error in MRI at the interface between difference phases, here between water and air. Although it cannot be entirely remedied, we have applied the correction mentioned in Saliba *et al.*[20]

However complex and costly, magnetic resonance velocimetry offers quantitative information about flow in optically inaccessible environments. In the flow case studied here, the liquid/gas interface acts as a hurdle in the optical path of light, which is completely circumvented by MRV.
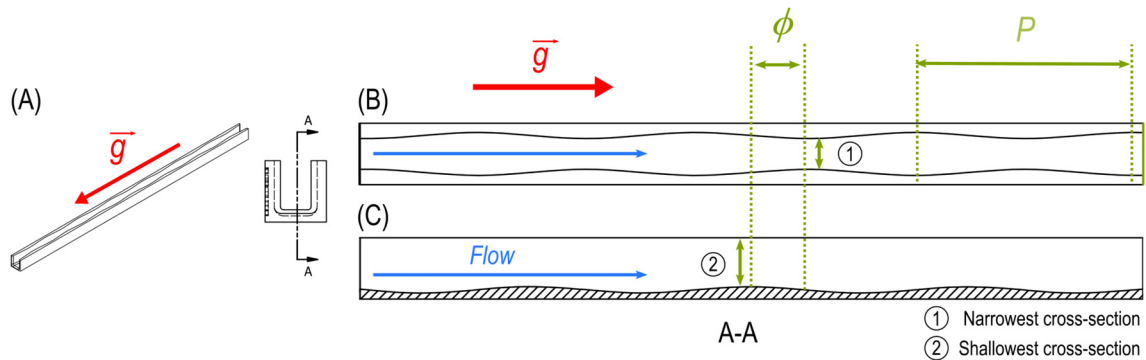

FIG. 1. Diagram of an open microchannel with a variable cross section. (a) Isometric view and front view (section with four periods), (b) top view, and (c) section A–A (section with four periods). The phase shift ϕ represents the distance between the narrowest section and the shallowest section. For example, if the phase shift is equal to zero, then the narrowest and shallowest sections coincide. In other words, the sinusoidal shapes along the bottom of the channel and along the sidewalls are in phase. The direction of flow is indicated with a blue arrow, and the direction of gravity is indicated with a red arrow. P is the period of the sine pattern.
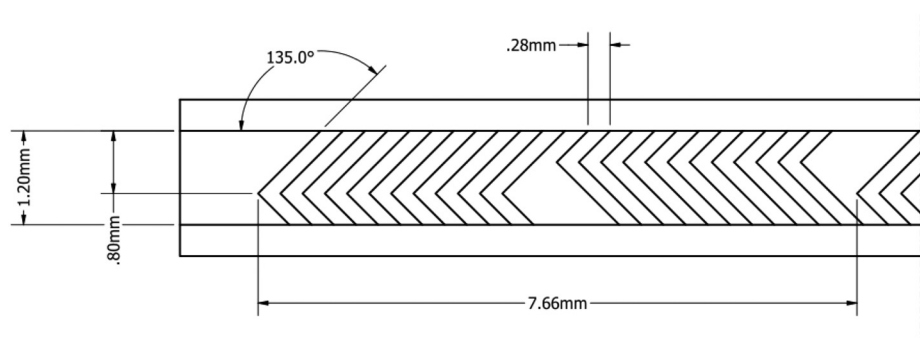
FIG. 2. Top view of a period of the open channel with herringbone grooves.

B. Experimental setup

The flow cells that we used to produce the falling films fit inside of a 10 mm test tube, which is then placed inside of an 11.7 T Bruker NMR system. A single high-performance liquid chromatography (HPLC) pump delivered water continuously to the test tube and then extracted it.

The open microchannels were made using two-photon polymerization. A photopolymer resin with a methacrylate reactive group was used to make the parts. This method is highly accurate but is not intended to print large structures, say, of a few centimeters. Only the microstructured part of the channel was printed in this way and was then placed in a larger support structure made out of polylactic acid (PLA) by fused filament fabrication (FFF). Figure 1 diagrams one such microstructured part. PTFE tubing is used to connect the pump to the inlet and outlet of the system. The support structure featured a hole to house the inlet tube and to lead it to the open channel. A groove covers the entire length of the back of the structure and holds the outlet tube.

The first set of designs have variable cross sections. More precisely, their width and depth vary as sine waves in the streamwise direction. Figure 1 shows one such channel. We studied the effect of the wavelength of the pattern and of the phase shift between the side walls and the bottom wall. We were also interested in the effect of channel geometry on the shape of the liquid/gas interface.

The basic cross section is a 1.4 mm wide rectangle with rounded edges. Viewed from the top, the sides of the channel have a sine-shape of amplitude 100 μm. The depth has a similar shape. Three different phase shifts between the width and depth sines were considered. Both sines had a phase shift of either 0°, 90°, or 180°. For each set of geometric parameters, volumetric flow rates of 0.75, 1.00, 1.50, and 2.00 mL min^{-1} were tested. In total, we investigated 24 distinct cases. Additionally, plain open-channels were also produced for comparison. These channels are straight in the streamwise direction, rectangular in cross section, and devoid of grooves. Three channels of width 1, 1.2, and 1.4 mm were made corresponding to the minimum, mean, and maximum width of the wavy channels.

We also tested straight channels with bas-relief chevron patterns. The patterns induce transverse motion which promotes mixing within the falling film. These channels will be designated as open-channel micromixers. The so-called staggered-herringbone patterns were first studied by Stroock et al.[23] for closed microchannels. They were later

on used by Al-Rawashdeh et al.[1] for falling-film microreactors, but without experimentally investigating the flow itself. Three different groove depths are considered here, namely, 50, 100, and 200 μm for channels that are 1200 μm wide (Fig. 2). Unlike closed-channel micromixers, the ratio of the groove depth to the channel height α cannot be specified beforehand since the height of the film depends on the flow rate and the geometry of the channel.

III. RESULTS

A. Wavy channels

We chose the surface-to-volume ratio S_v to evaluate the falling-film microreactors since it quantifies the shape of the film; a thinner film with a larger interfacial area means higher performance. Figure 3 gives an overview of the performance of the six geometrical configurations as a function of volumetric flow rates. We chose these volumetric flow rates since at the lower end, the film becomes so thin that breaks up for certain cases. Since the films are thicker for higher volumetric flow rates, all of the configurations result in nearly the same overall surface-to-volume ratio, indicating that any effect of the
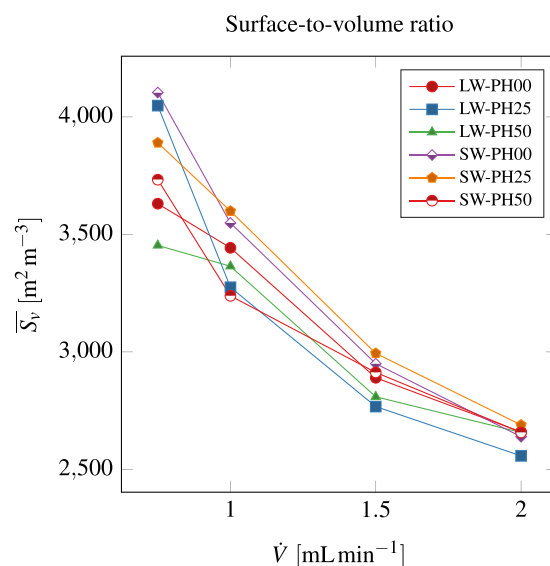

FIG. 3. Overall surface-to-volume ratio for the six wavy channels presented in Table I as a function of volumetric flow rate.
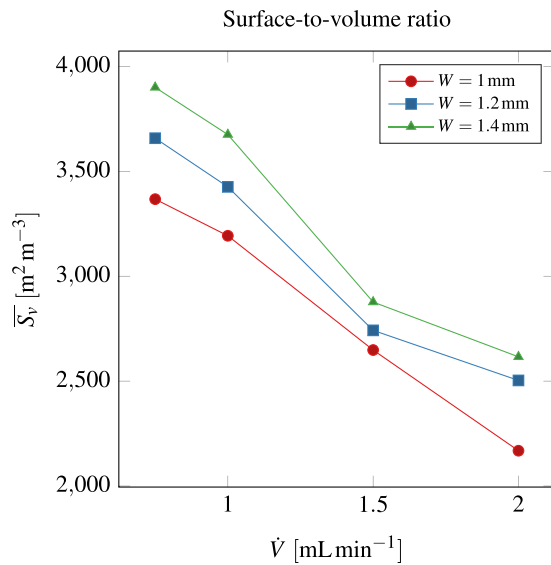
Surface-to-volume ratio

FIG. 4. Overall surface-to-volume ratio for straight channels with different widths as a function of volumetric flow rate.

microstructures on the liquid–gas interface is negligible compared to the volume of the film. The cases begin to differentiate themselves from one another as the volumetric flow rate is decreased, revealing some notable patterns. It is difficult to deduce a pattern from the data in Fig. 3 as to the effect of phase shift on the surface-to-volume ratio. The surface-to-volume ratios inside of straight channels that are 1, 1.2, and 1.4 mm wide (corresponding to the minimum, mean, and maximum widths of the patterned channels) are plotted in Fig. 4. As was expected, the narrowest channel produces the lowest surface-to-volume ratio. Most of the results in Fig. 3 fall between curves $W = 1$ mm and $W = 1.4$ mm in Fig. 4 for higher volumetric flow rates, before overcoming the latter curve for lower mass flow rates.

1. Long wavelength channels

To try and unpack some of these observations, the surface-to-volume ratios of the cross sections of the film at different axial positions are plotted in Fig. 5. These plots show the variations of the flow within the wavy channels. Figures 5(a)–5(c) show that the surface-to-volume ratio fluctuates in a similar way for the three phase shifts, but with different amplitudes. This becomes more apparent in Fig. 7(a), where additional data from a channel with a flat bottom surface, referred to as the "single sine" case, is included. The figure also shows the channel width in arbitrary units (a.u.) for reference. Among the cases studied, the amplitude reaches its highest value for $\phi = 0.5$ and its lowest for $\phi = 0$. For $\phi = 0.25$, the surface-to-volume ratio has a minimum value of S_v that is higher than for all other cases, while its maximum value aligns closely with those of the $\phi = 0.5$ case and the "single sine" reference.

Figure 6 presents the thickness profile along the axial direction as a function of the dimensionless position z/P. The profiles show that, regardless of the value of ϕ, the overall shapes remain similar, differing in the amplitude of fluctuations. A phase shift of $\phi = 0.5$ results in the highest peak thickness among the cases studied, with one exception: at a flow rate of $\dot{V} = 1.00$ mL min^{-1}, the peak thickness is comparable across all phase shifts. Meanwhile, for $\phi = 0$ and $\phi = 0.25$, the thickness profiles nearly overlap for most flow rates, except at $\dot{V} = 0.75$ mL min^{-1}. At this lower flow rate, the profile for $\phi = 0$ deviates significantly, which is attributable to film breakup.

Figure 7(a) compares the different cases at the same flow rate of $\dot{V} = 2.00$ mL min^{-1}. The surface-to-volume ratio and thickness profiles across all cases resemble the reference "single sine" profile, whose bottom wall is flat. The similarity in shape underscores the dominant influence of the channel's side walls on the flow characteristics. However, the magnitude of the values varies significantly among the cases. For instance, the thickness is higher for $\phi = 0.5$ and lower for $\phi = 0.25$, indicating that the depth of the channel amplifies or attenuates the effects of the side walls. In sum, for long wavelengths, the side
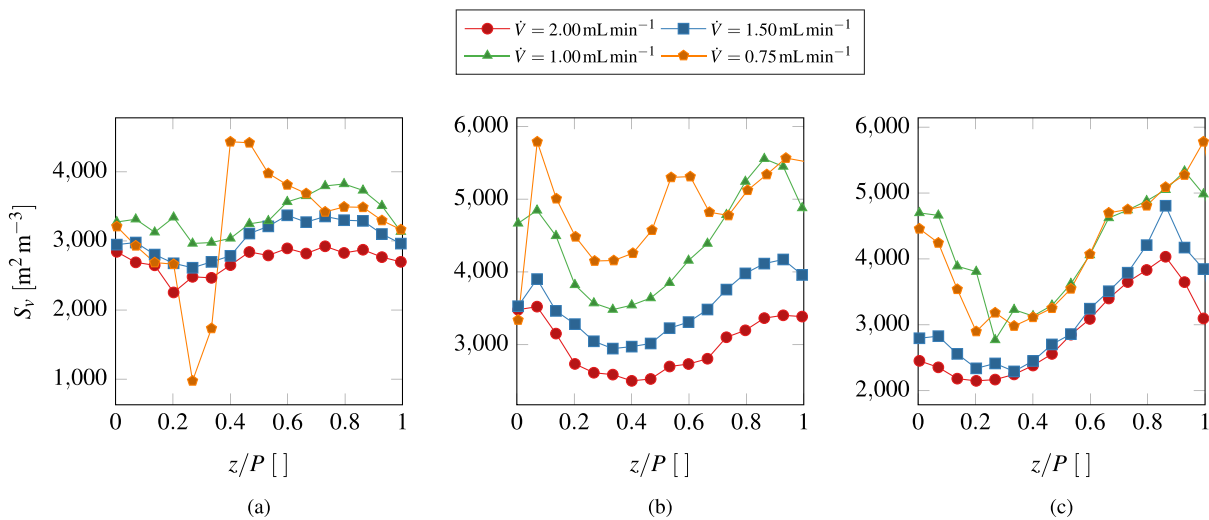

FIG. 5. Long wavelength channel: local surface-to-volume ratio along the axial direction for (a) $\phi = 0$, (b) $\phi = 0.25$, and (c) $\phi = 0.5$. The axial position z was non-dimensionalized using the period of the spatial pattern P.
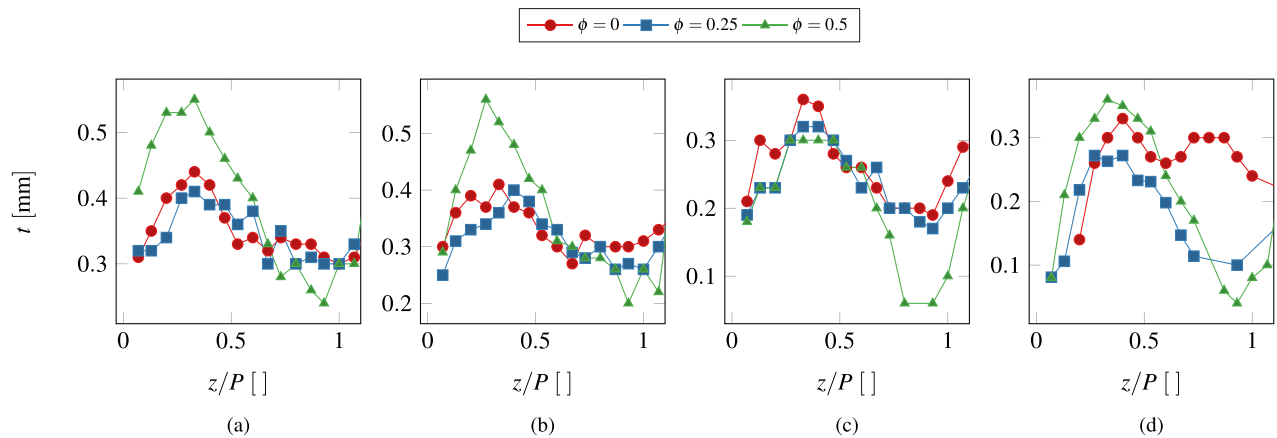
FIG. 6. Long wavelength channel: local minimum thickness of the film along the axial direction for volumetric flow rates: (a) $2.00\,\text{mL}\,\text{min}^{-1}$, (b) $1.50\,\text{mL}\,\text{min}^{-1}$, (c) $1.00\,\text{mL}\,\text{min}^{-1}$, and (d) $0.75\,\text{mL}\,\text{min}^{-1}$. The axial position z was non-dimensionalized using the period of the spatial pattern P.

walls stretch and compress the film modulating its cross section, while the bottom of the channel has a lesser influence on the shape of the flow. This is not the case if the wavelength is shorter, since the interplay between the side walls and the bottom wall is more pronounced.

2. Short wavelength channels

Figure 8 presents the surface-to-volume ratio of the liquid film flowing through short wavelength channels as a function of the
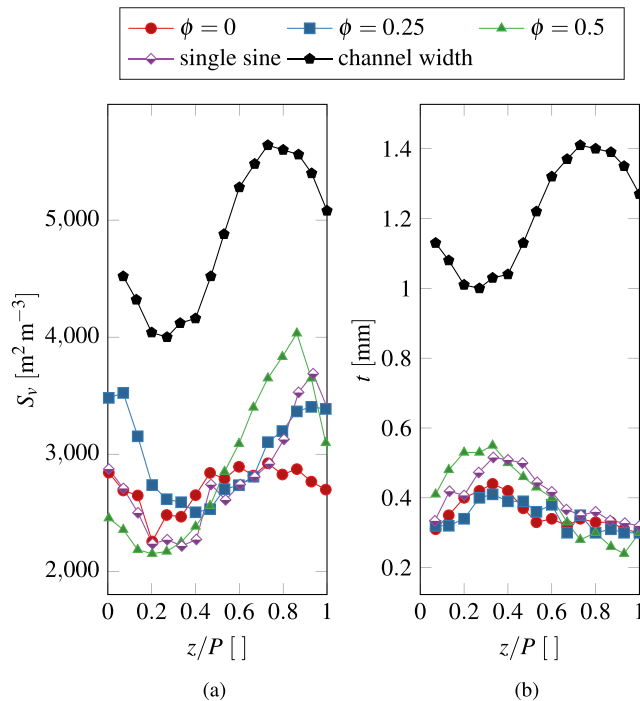

FIG. 7. Long wavelength channels: comparison of (a) local surface-to-volume ratio and (b) minimum thickness profile for different channel geometries at $\dot{V} = 2\,\text{mL}\,\text{min}^{-1}$.

volumetric flow rate. Unlike the long wavelength channels, the results here show that the phase shift affects the shape of the film. While the features of the curves remained at the same axial position for a longer wavelength, regardless of the value of ϕ, the profiles of S_v for short wavelengths become shifted. The maximum channel width is approximately centered in the plot at $z/P = 0.5$, as seen in Fig. 9(b). When the phase shift $\phi = 0$, this central point aligns with the trough at the bottom of the channel, with the surface-to-volume ratio peaking slightly before this trough. However, when $\phi = 0.25$, the channel depth reaches its maximum at $z/P = 0.75$, corresponding to a position one-fourth of a period after the widest channel location. The surface-to-volume ratio reflects this change, with its peak occurring just prior to this maximum depth, around $\phi = 0.7$. A further phase shift to $\phi = 0.5$ produces a different scenario, where the peak nearly coincides with the point of maximum channel width and minimum depth at $z/P = 0.5$.

The thickness profiles in Fig. 10 further illustrate the influence of the short wavelength pattern on flow behavior. Unlike the long wavelength channels, where the thickness profiles follow consistent shapes, the short wavelength introduces significant displacement of the peaks and troughs. The locations of maximum and minimum thickness shift depending on the phase shift. A phase shift of $\phi = 0.5$ results in the most pronounced amplitude of fluctuation among the profiles. The other profiles, corresponding to different phase shifts, span comparable ranges of thickness, except for the lowest flow rate for which the profile for $\phi = 0.25$ is thinner than for $\phi = 0$.

We then compared the surface-to-volume ratio and thickness profiles for a fixed volumetric flow rate of $\dot{V} = 2\,\text{mL}\,\text{min}^{-1}$ with the results from a channel with a flat bottom surface. Unlike the long wavelength channels, where certain cases overlapped with the "single sine" reference case, none of the short wavelength scenarios showed overlap. This suggests that the short wavelength geometry accentuates the effects of the bottom wall on the flow.

B. Chaotic micromixers

The micromixers studied here produced a steady three-dimensional flow that is periodic in the axial $z-$ direction. Based on
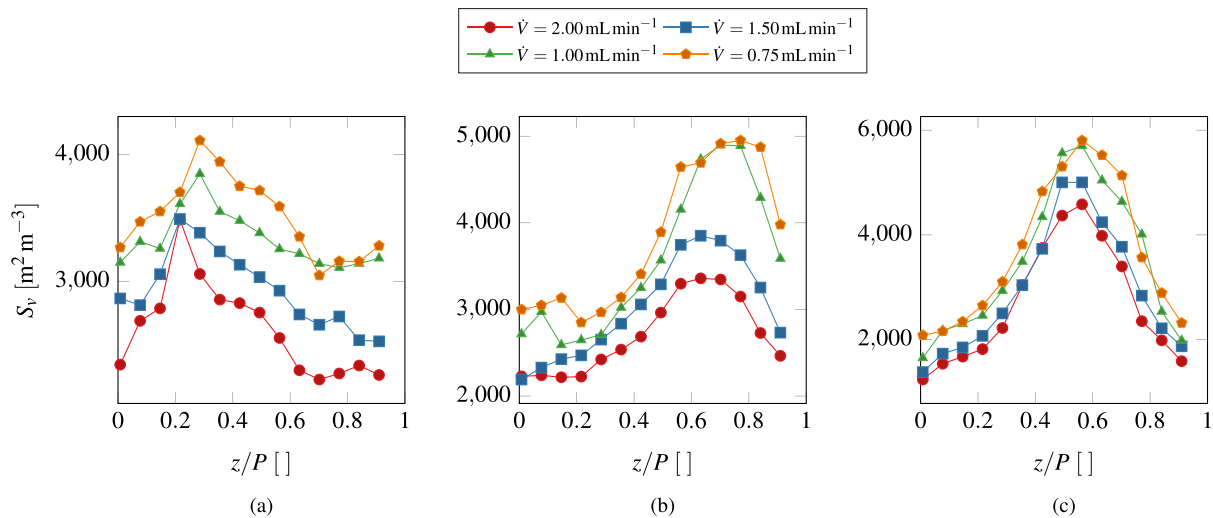
FIG. 8. Short wavelength channel: local surface-to-volume ratio along the axial direction for (a) $\phi = 0$, (b) $\phi = 0.25$, and (c) $\phi = 0.5$. The axial position z was non-dimensionalized using the period of the spatial pattern P.

the linked twist map theory proposed by Sturman et al.,[24] the back-and-forth displacement of the vortex centers in the transverse $xy-$plane guarantees that the fluid particles follow chaotic trajectories. Unlike closed-channel micromixers, the height of the flow depends on the volumetric flow rate, and so does the intensity of the transverse
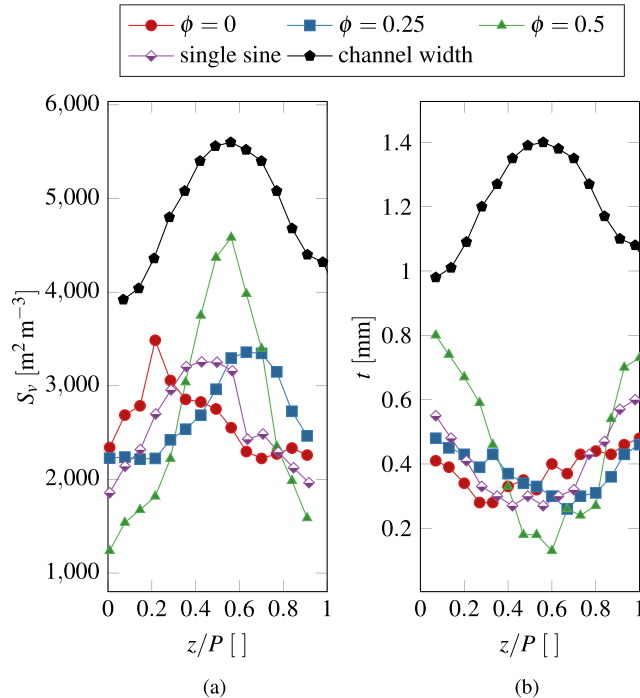

FIG. 9. Short wavelength channels: comparison of (a) local surface-to-volume ratio and (b) minimum thickness profile for different channel geometries at $\dot{V} = 2\,\text{mL min}^{-1}$.

motion. As detailed in Ottino,[19] Poincaré sections reveal the regions in the flow where mixing is the most efficient. These sections are a super-position of the intersections of the flow streamlines with planes placed at the end of each cycle. The data presented here does not lend itself to this procedure since it covers at most a single period of the spatial pattern. It could be imagined that, since the flow is periodic, one could stack the data in the $z-$ direction to obtain several cycles of the flow and then compute the streamlines. However, a much simpler way, which avoids patching the data and accumulating errors, consists in plotting the streamlines for one half-cycle and projecting them onto the transverse plane. In the end, the presence of the vortices and magnitude of the transverse velocity vector are what determine the mixing efficiency. Figure 11 shows an example of the visualization used to present the flow inside of the micromixer. The figure shows streamlines stemming from a single straight line in the inlet plane of the flow, indicated in red. The streamlines reveal the motion due to the vortex pair which is first centered to the left. As the tip of the groove pattern moves downstream to the right, so does the center of the two vortices, indicated here by an arrow. Figure 12 shows the project streamlines for three different groove depths (50, 100, and 200 μm) and four different volumetric flow rates (1, 2, 3, and 4 mL min^{-1}). We chose this range of volumetric flow rates in order to cover a range of groove depth to film thickness that is comparable to the literature on closed-channel micromixers. Unlike Fig. 11, the streamlines in Fig. 12 stem from a grid of points filling the entire inlet plane. The flow patterns, however, are similar in both figures.

As mentioned before, the streamlines are plotted for a single half-cycle, and the tip of the chevron pattern is on the right side, meaning that the border separating the two vortices, if they are present, is on the right side of the cross-sectional view. As expected for all the cases, the streamlines at the bottom of the channels indicate that the grooves deviate the flow, but do not lead to clear vortex structures if the grooves are 50 μm deep. To make this even clearer, the streamlines are colored by the intensity of the $x-$ component (horizontal) of the velocity field. The 50 μm deep grooves do not result in noticeable
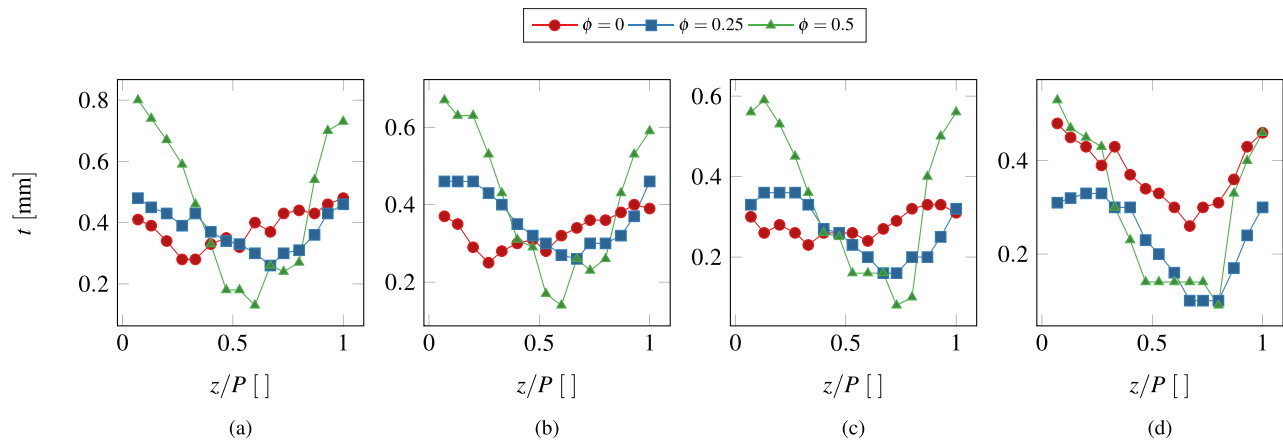
FIG. 10. Short wavelength channel: local minimum thickness of the film along the axial direction for volumetric flow rates: (a) $2.00\,\mathrm{mL\,min^{-1}}$, (b) $1.50\,\mathrm{mL\,min^{-1}}$, (c) $1.00\,\mathrm{mL\,min^{-1}}$, and (d) $0.75\,\mathrm{mL\,min^{-1}}$. The axial position z was non-dimensionalized using the period of the spatial pattern P.

vortex pairs, regardless of volumetric flow rate. Aside from the flow in the grooves at the bottom of the channel, the transverse component of the flow is negligible in most of the cross section. With deeper grooves, two counter-rotating vortex regions stand out. For a depth of $100\,\mu m$, the vortex pair is present at $\dot{V} = 1\,\mathrm{mL\,min^{-1}}$ and becomes more noticeable for $\dot{V} = 2\,\mathrm{mL\,min^{-1}}$. Starting at $\dot{V} = 3\,\mathrm{mL\,min^{-1}}$, and as the film continues to become thicker, the vortex pair is confined to the bottom of the channel, near the grooves. For the highest flow rate, the streamlines begin to resemble those of the case with shallow grooves. For grooves $200\,\mu m$ deep, the vortex pair occupies the entirety of the film for all volumetric flow rates. The velocity in the $x-$ direction in the top half of the film is opposite to that at the bottom, which denotes the presence of a vortex.

Worth noting is that the grooves do not affect the surface-to-volume ratio, nor the shape of the interface. As an example, Fig. 13 shows the surface-to-volume ratio for a groove depth of $100\,\mu m$ and $\dot{V} = 3\,\mathrm{mL\,min^{-1}}$. The surface-to-volume profile remains flat, and the periodicity of the grooves is not reflected in the surface.

In addition to visualizing the flow, we also need an overall quantitative assessment of the mixing efficiency. Studies on micromixers, which often use dyes, look at the uniformity of the dye at given cross sections. Similarly, some numerical studies resort to tracking the position of virtual particles and determining their distribution. The literature on micromixers also offers concepts carried over from chaos theory, most notably the Lyapunov exponent. In a nutshell, particles in the flow that are initially close to one another will diverge at an exponential rate if their trajectories are chaotic. The Lyapunov exponent is the rate at which these particles grow apart. In an experimental setting, Wolf et al.[26] proposed an algorithm that computes the Lyapunov exponent by constantly resetting the distance between two particles, one of which is a reference particle, once it exceeds a certain amount. This approach was problematic since the choice of the initial distance between the particles and the maximum distance are arbitrary. Additionally, the algorithm was sensitive to noise, in the sense that some trajectories would suddenly diverge at a very large rate, leading to large value of the exponent and affecting the average value. Filtering these trajectories involves an arbitrary cutoff.

For these reasons, we chose the helicity of the flow field to evaluate mixing. Unlike closed-channel flows, the volume V of liquid in the field of view depends on the volumetric flow rate, and so the total helicity was divided by the volume of the film. In the end, the helicity per unit volume is given by

$$\mathscr{H} = \frac{1}{V}\int_V \mathbf{u}\cdot(\nabla\times\mathbf{u})dv = \frac{1}{V}\int_V \mathbf{u}\cdot\boldsymbol{\omega}\,dv, \qquad (8)$$

where ω is the vorticity, and v is an volume element.

Figure 14 shows $\mathscr{H}$ as a function of the volumetric flow rate. As expected, the channel whose grooves are $50\,\mu m$ deep performs the worst. The average helicity for the remaining two cases are comparable, with the $100\,\mu m$ grooves ahead for the lower volumetric flow rates before being caught up and surpassed by the last case for higher rates, which agrees with observations from Fig. 12. The vortex pair started to fade away for higher volumetric flow rates for a depth of $100\,\mu m$, whereas it remained for $200\,\mu m$.
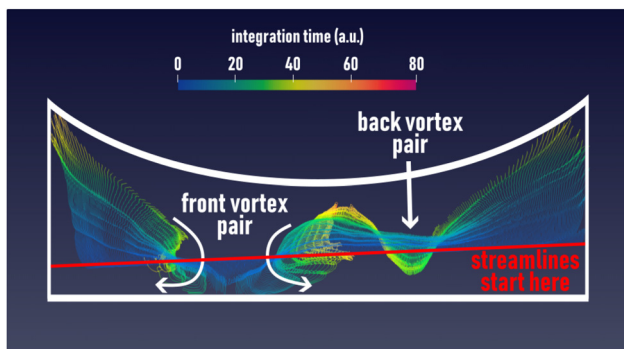

FIG. 11. Axial view of the streamlines computed from the velocity field of an open-channel micromixer starting from a line indicated in red. The direction of rotation of the vortex pair to the left is indicated by arrows. The vortex pair then moves to the right in the back. The streamlines are colored by integration time in arbitrary units.
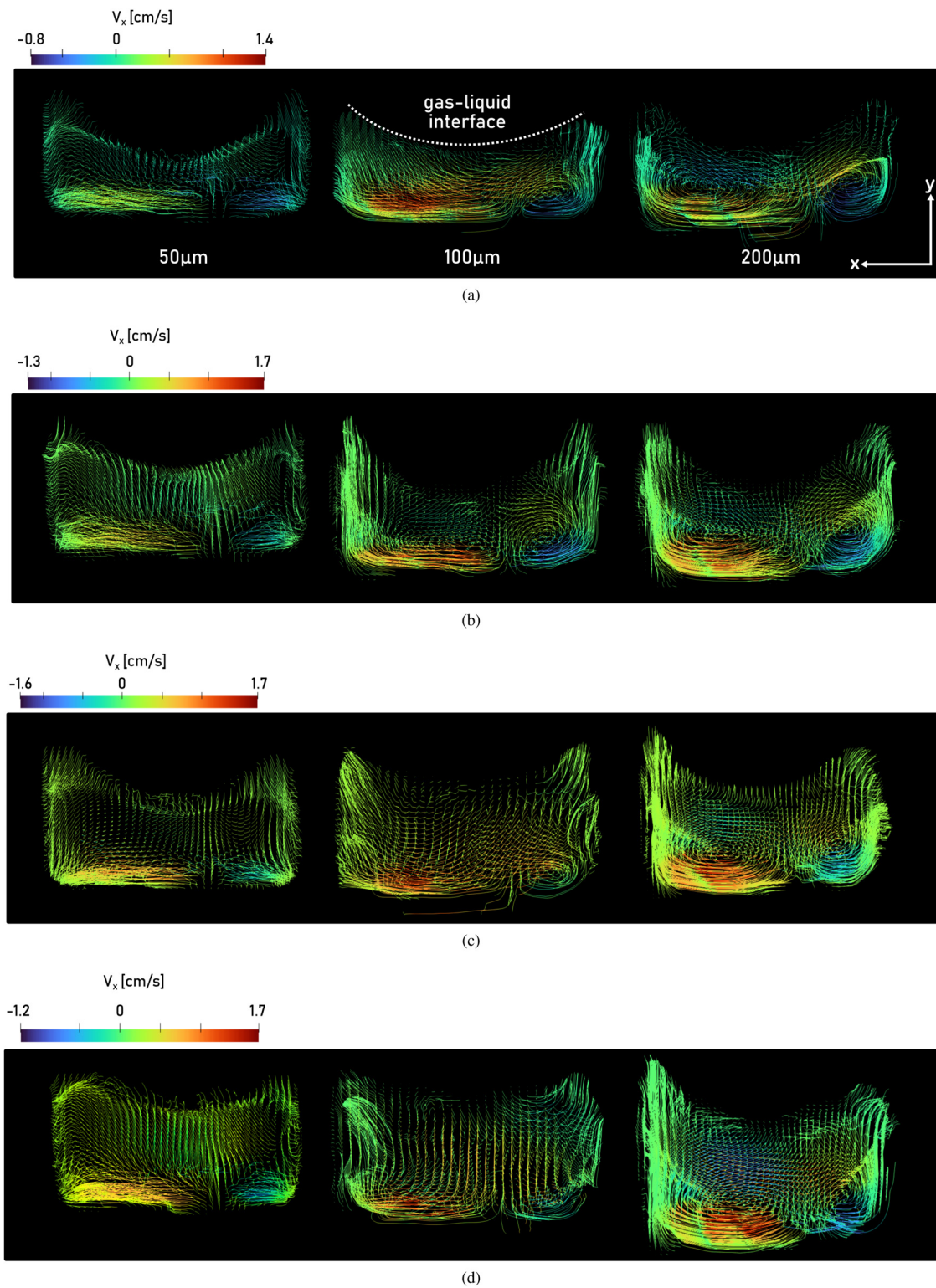
FIG. 12. Streamlines seeded on a uniform grid obtained from experimental MR velocimetry measurements for different groove depths for volumetric flow rates of (a) 1.00 mL min^{-1}, (b) 2.00 mL min^{-1}, (c) 3.00 mL min^{-1}, and (d) 4.00 mL min^{-1}.
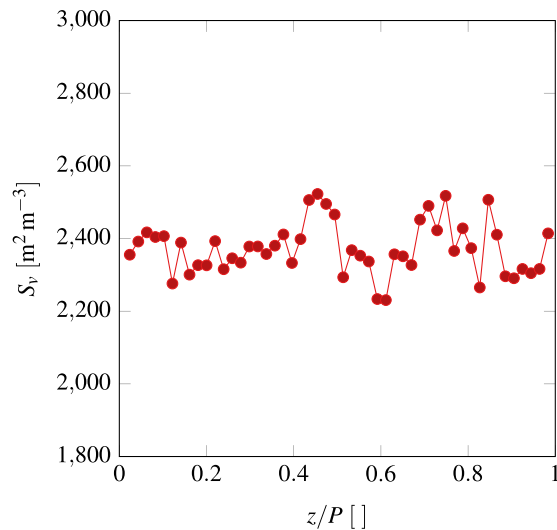
FIG. 13. Local surface-to-volume ratio along a herringbone mixer with groove depth of 100 μm and volumetric flow rate of 3 mL min^{-1}.

We can describe the evolution of the vortex pairs using the ratio of the groove depth to film thickness α. The literature on closed-channel staggered-herringbone micromixers stresses the importance of α (here channel height would replace film thickness). In the seminal work on staggered-herringbone mixers, Stroock et al.[23] used a ratio $\alpha = 0.23$ for all the experiments. Building on that work, Aubin et al.[5] used the same channel design with additional values of $\alpha = 0.30$ and 0.35 and found that mixing efficiency improves with α. Ianovska et al.[15] explored a wide range of values with $\alpha = 0.22$, 0.37, and 0.83 and arrived at a similar conclusion. Other studies where vortex pairs were observed have ratios falling in the range $\alpha = 0.2$–1.0 ($\alpha = 0.5$,[28] 1.0,[25] and 0.1–0.94[14]). We computed the ratio α for the different cases
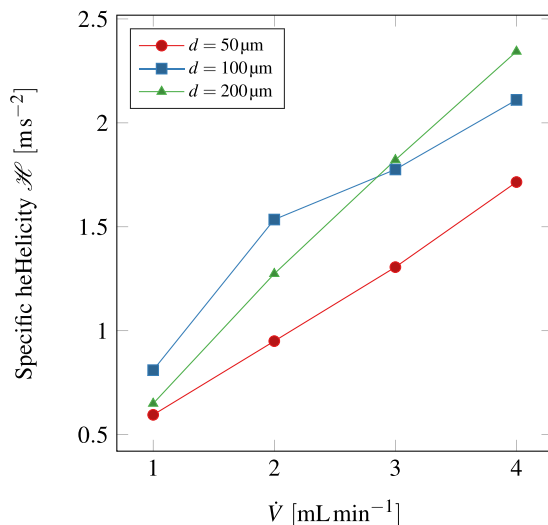

FIG. 14. The specific helicity as a function of volumetric flow rate for different groove depths.
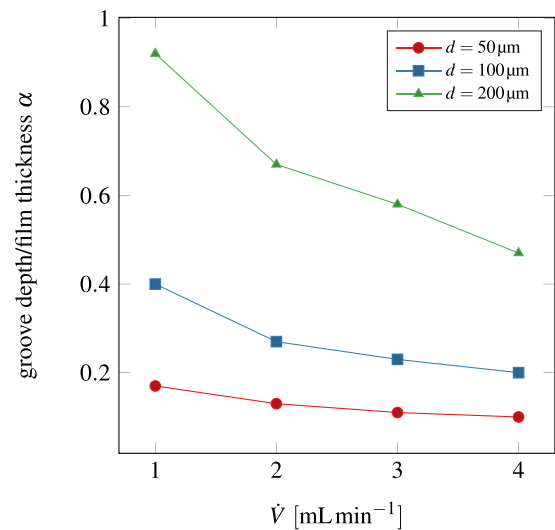

FIG. 15. Ratio of groove depth to minimum film thickness as a function of volumetric flow rate.

of Fig. 12 where the minimum thickness of the film stands in for channel height. The minimum thickness is the distance between the bottom of the meniscus (gas/liquid interface) and the top of the ridges (not the bottom of the grooves). Figure 15 presents the values of α for the different groove depths as a function of volumetric flow rate. The ratio α spans a range of 0.1–0.92. As expected, for $d = 50\,\mu$m, α is much lower than for the other cases, in the range of 0.1–0.17, which would explain the absence of a vortex pair. For $d = 100\,\mu$m, $\alpha = 0.40$ for the lowest volumetric flow rate and decreases to 0.20 at the highest, approaching the values of $d = 50\,\mu$m, for which vortices are absent. For the deepest grooves $d = 200\,\mu$m, the ratio is equal to or greater than 0.47, reaching up to 0.92 for $\dot{V} = 1.00$ mL min^{-1}. Even though the microchannel flow has a free surface, the results agree with the literature on closed channels.

IV. CONCLUSION

In the present work, we have investigated falling films inside of open microchannels using magnetic resonance velocimetry. This method is non-intrusive, and its main constraint in the context of microfluidics is that it is incompatible with magnetic materials. It offers information from within the flow without the need to introduce seeding particles that can alter the physical properties of the fluid under investigation. We have used magnetic resonance technology to measure velocity fields within a flowing liquid, but the same equipment can resolve temperature and concentration distributions in space.

We studied first how periodic width and depth variations affect the shape of the film, which we quantified using the surface-to-volume ratio. We found that if the wavelength of the pattern is long, then the surface-to-volume and film thickness distributions are qualitatively similar, regardless of the phase shift between the sinusoidal width and depth patterns. The phase shift mainly affected the amplitude of variation. For a shorter wavelength, the phase shift changed how the thickness of the film is distributed along the axial direction. A phase shift of 0.5 also resulted in the worst performance. Although they had different thickness and surface-to-volume ratio profiles, the remaining cases

had a similar overall surface-to-volume ratio. The gain in S_v from reducing the flow rate surpasses by far any improvement due to the geometry.

We then investigated the three-dimensional, three-component flow inside of an open-channel chaotic micromixer. We showed that the grooves do not affect the surface-to-volume ratio in that it remains the same along the axial direction. In accordance with observations in the literature, the depth of the grooves also plays a big role in mixing for open microchannels. For a depth of at least $100\,\mu m$, we observed vortex pairs in the flow that carry liquid from the gas/liquid interface to the bottom of the channel. The results agree with the literature on closed-channel staggered-herringbone micromixers.

The current work does not claim to exhaustively investigate the geometric parameters that affect both flow cases. However, it shows the detailed information that magnetic resonance technology can provide, without having to make assumptions about the flow or adding seeding particles that can disrupt it or changes its properties. This data allows us to comprehensively test complex designs and then reiterate them toward optimal performance. We also showed how advanced microstructuring techniques can be applied to structure both the shape of the liquid gas interface as well as the complex flow within the falling film. The ability to measure temperature and chemical concentrations using the same device also offers attractive possibilities to observe different aspects of the flow. This information can guide the design of industrial or lab-scale falling-film devices to improve their efficiency based on firm experimental results.

ACKNOWLEDGMENTS

AUTHOR DECLARATIONS

Conflict of Interest

The authors have no conflicts to disclose.

Author Contributions

Georges C. Saliba: Conceptualization (equal); Formal analysis (equal); Investigation (equal); Methodology (equal); Validation (equal); Writing – original draft (equal); Writing – review & editing (equal). **Jan G. Korvink:** Conceptualization (equal); Funding acquisition (equal); Writing – review & editing (equal). **Juergen J. Brandner:** Conceptualization (equal); Funding acquisition (equal); Writing – review & editing (equal).

DATA AVAILABILITY

The data that support the findings of this study are available from the corresponding author upon reasonable request.

REFERENCES

[1] M. Al-Rawashdeh, A. Cantu-Perez, D. Ziegenbalg, P. Löb, A. Gavriilidis, V. Hessel, and F. Schönfeld, "Microstructure-based intensification of a falling film microreactor through optimal film setting with realistic profiles and in-channel induced mixing," Chem. Eng. J. **179**, 318–329 (2012).

[2] M. Al-Rawashdeh, V. Hessel, P. Löb, K. Mevissen, and F. Schönfeld, "Pseudo 3-D simulation of a falling film microreactor based on realistic channel and film profiles," Chem. Eng. Sci. **63**, 5149–5159 (2008).

[3] M. A. Ansari and K.-Y. Kim, "Shape optimization of a micromixer with staggered herringbone groove," Chem. Eng. Sci. **62**(23), 6687–6695 (2007).

[4] J. Aubin, D. F. Fletcher, J. Bertrand, and C. Xuereb, "Characterization of the mixing quality in micromixers," Chem. Eng. Technol. **26**(12), 1262–1270 (2003).

[5] J. Aubin, D. F. Fletcher, and C. Xuereb, "Design of micromixers using CFD modelling," Chem. Eng. Sci. **60**(8–9), 2503–2516 (2005).

[6] B. Boga, K. Baur, V.-M. Cristea, N. Steinfeldt, and N. Kockmann, "Experimental and numerical investigations of flow behavior in an open falling film microreactor equipped with curved flow splitting elements," Chem. Eng. Sci. **298**, 120338 (2024a).

[7] B. Boga, K. Baur, E.-C. Timiş, H. Lund, T. Peppel, V.-M. Cristea, N. Kockmann, and N. Steinfeldt, "Photocatalytic antibiotic degradation in coated open microchannels by applying 2D and 3D flow modeling with kinetics," J. Environ. Chem. Eng. **12**(6), 114173 (2024b).

[8] S. Chen, T. Zhang, L. Lv, Y. Chen, and S. Tang, "Simulation of the hydrodynamics and mass transfer in a falling film wavy microchannel," Chin. J. Chem. Eng. **34**, 97–105 (2021).

[9] Y. Du, Z. Zhang, C. Yim, M. Lin, and X. Cao, "A simplified design of the staggered herringbone micromixer for practical applications," Biomicrofluidics **4**(2), 024105 (2010).

[10] C. L. Dumoulin, S. P. Souza, R. D. Darrow, N. J. Pelc, W. J. Adams, and S. A. Ash, "Simultaneous acquisition of phase-contrast angiograms and stationary-tissue images with hadamard encoding of flow-induced phase shifts," J. Magn. Reson. Imaging **1**, 399–404 (1991).

[11] H. Ehrich, D. Linke, K. Morgenschweis, M. Baerns, and K. Jähnisch, "Application of microstructured reactor technology for the photochemical chlorination of alkylaromatics," Chimia **56**(11), 647 (2002).

[12] C. J. Elkins and M. T. Alley, "Magnetic resonance velocimetry: Applications of magnetic resonance imaging in the measurement of fluid motion," Exp. Fluids **43**, 823–858 (2007).

[13] E. Fukushima, "Nuclear magnetic resonance as a tool to study flow," Annu. Rev. Fluid Mech. **31**, 95–123 (1999).

[14] D. Hassell and W. Zimmerman, "Investigation of the convective motion through a staggered herringbone micromixer at low Reynolds number flow," Chem. Eng. Sci. **61**(9), 2977–2985 (2006).

[15] M. A. Ianovska, P. P. F. A. Mulder, and E. Verpoorte, "Development of small-volume, microfluidic chaotic mixers for future application in two-dimensional liquid chromatography," RSC Adv. **7**(15), 9090–9099 (2017).

[16] K. Jähnisch, M. P. D. Baerns, V. Hessel, W. Ehrfeld, V. Haverkamp, H. Löwe, C. Wille, and A. E. Guber, "Direct fluorination of toluene using elemental fluorine in gas/liquid microreactors," J. Fluorine Chem. **105**, 117 (2000).

[17] C.-P. Jen, C.-Y. Wu, Y.-C. Lin, and C.-Y. Wu, "Design and simulation of the micromixer with chaotic advection in twisted microchannels," Lab Chip **3**(2), 77–81 (2003).

[18] T. J. Kwak, Y. G. Nam, M. A. Najera, S. W. Lee, J. R. Strickler, and W.-J. Chang, "Convex grooves in staggered herringbone mixer improve mixing efficiency of laminar flow in microchannel," PLoS One **11**(11), e0166068 (2016).

[19] J. M. Ottino, Cambridge Texts in Applied Mathematics: The Kinematics of Mixing: Stretching, Chaos, and Transport Series Number 3 (Cambridge University Press, Cambridge, England, 1989).

[20] G. C. Saliba, J. G. Korvink, and J. J. Brandner, "Magnetic resonance velocimetry of thin falling films," Chem. Eng. J. **498**, 155260 (2024a).

[21] G. C. Saliba, J. G. Korvink, and J. J. Brandner, "Magnetic resonance velocimetry reveals secondary flow in falling films at the microscale," Phys. Fluids **36**(7), 071705 (2024b).

[22] F. Schönfeld and S. Hardt, "Simulation of helical flows in microchannels," AIChE J. **50**(4), 771–778 (2004).

[23] A. D. Stroock, S. K. Dertinger, A. Ajdari, I. Mezic, H. A. Stone, and G. M. Whitesides, "Chaotic mixer for microchannels," Science **295**(5555), 647–651 (2002).

[24] R. Sturman, J. M. Ottino, and S. Wiggins, The Mathematical Foundations of Mixing: The Linked Twist Map as a Paradigm in Applications: Micro to Macro, Fluids to Solids (Cambridge University Press, 2006).

[25]E. Tóth, E. Holczer, K. Iván, and P. Fürjes, "Optimized simulation and validation of particle advection in asymmetric staggered herringbone type micromixers," Micromachines **6**(1), 136–150 (2014).

[26]A. Wolf, J. B. Swift, H. L. Swinney, and J. A. Vastano, "Determining lyapunov exponents from a time series," Phys. D **16**(3), 285–317 (1985).

[27]T. Xie, C. Zeng, C. Wang, and L. Zhang, "Preparation of methyl ester sulfonates based on sulfonation in a falling film microreactor from hydrogenated palm oil methyl esters with gaseous SO3," Ind. Eng. Chem. Res. **52**(10), 3714–3722 (2013).

[28]J.-T. Yang, K.-J. Huang, and Y.-C. Lin, "Geometric effects on fluid mixing in passive grooved micromixers," Lab Chip **5**(10), 1140–1147 (2005).

[29]K. K. Yeong, A. Gavriilidis, R. Zapf, and V. Hessel, "Experimental studies of nitrobenzene hydrogenation in a microstructured falling film reactor," Chem. Eng. Sci. **59**, 3491–3494 (2004).

[30]H. Zhang, G. Chen, J. Yue, and Q. Yuan, "Hydrodynamics and mass transfer of gas-liquid flow in a falling film microreactor," AIChE J. **55**, 1110–1120 (2009).

[31]D. Ziegenbalg, P. Löb, M. Al-Rawashdeh, D. Kralisch, V. Hessel, and F. Schönfeld, "Use of 'smart interfaces' to improve the liquid-sided mass transport in a falling film microreactor," Chem. Eng. Sci. **65**, 3557–3566 (2010).

30 April 2025 10:38:37